Lawrence Berkeley National Laboratory
LBL Publications

Title
Coupled thermal-hydrological-mechanical behavior of rock mass surrounding a high-temperature thermal energy storage cavern at shallow depth

Permalink
https://escholarship.org/uc/item/9xx1n458

Authors
Park, Jung-Wook
Rutqvist, Jonny
Ryu, Dongwoo
et al.

Publication Date
2016-03-01

DOI
10.1016/j.ijrmms.2016.01.007

Peer reviewed

Coupled Thermal-Hydrological-Mechanical Behavior of Rock Mass Surrounding a High-Temperature Thermal Energy Storage Cavern at Shallow Depth

Jung-Wook Park[a*], Jonny Rutqvist [b], Dongwoo Ryu[a], Eui-Seob Park[a], Joong-Ho Synn[a]

[a] Geologic Environment Division, Korea Institute of Geoscience and Mineral Resources (KIGAM), Gwahang-no 124, Yuseong-gu, Daejeon 305-350, Republic of Korea
[b] Earth Sciences Division, Lawrence Berkeley National Laboratory, Berkeley, CA 94720, USA

* Corresponding author
Jung-Wook Park
E-mail: jwpark@kigam.re.kr
Telephone: +82-42-868-3246
Fax: +82-42-868-3416

Abstract

The present study is aimed at numerically examining the thermal-hydrological-mechanical (THM) processes within the rock mass surrounding a cavern used for thermal energy storage (TES). We considered a cylindrical rock cavern with a height of 50 m and a radius of 10 m storing thermal energy of 350ºC as a conceptual TES model and simulated its operation for 30 years using THM coupled numerical modeling. At first, the insulator performance was not considered for the purpose of investigating the possible coupled THM behavior of the surrounding rock mass; then, the effects of an insulator were examined for different insulator thicknesses. The key concerns were focused on the hydro-thermal multiphase flow and heat transport in the rock mass around the thermal storage cavern, the effect of evaporation of rock mass, thermal impact on near the ground surface and the mechanical behavior of the surrounding rock mass. It is shown that the rock temperature around the cavern rapidly increased in the early stage and, consequently, evaporation of groundwater occurred, raising the fluid pressure. However, evaporation and multiphase flow did not have a significant effect on the heat transfer and mechanical behavior in spite of the high-temperature (350ºC) heat source. The simulations showed that large-scale heat flow around a cavern was expected to be conduction-dominated for a reasonable value of rock mass permeability. Thermal expansion as a result of the heating of the rock mass from the storage cavern led to a ground surface uplift on the order of a few centimeters and to the development of tensile stress above the storage cavern, increasing the potentials for shear and tensile failures after a few years of the operation. Finally, the analysis showed that high tangential stress in proximity of the storage cavern can some shear failure and local damage, although large rock wall failure could likely be controlled with appropriate insulators and reinforcement.

Key words: Thermal-hydrological-mechanical coupled analysis, Thermal energy storage, Rock cavern, TOUGH-FLAC simulator

1. Introduction

The effective management of existing energy resources is as important as the development of new energy sources. Energy storage systems make it possible to use renewable energy sources for heating and cooling, in addition to power generation when required, by remedying the problems resulting from their intermittent and variable characteristics. An energy storage system can balance the energy demand and supply, thus improving the overall efficiency and flexibility of energy systems.

Thermal energy storage (TES) is an energy storage technology, which stores thermal resources, such as solar energy, geothermal energy and industrial waste heat, without converting the thermal resource into different forms of energy. In general, above-ground TES has been commercially used in concentrating solar power (CSP) plants, but little attention has been paid to the applicability of a rock cavern to large-scale high-temperature thermal energy storage, except for a few studies (Park et al. 2013; Park et al. 2014; Kim et al. 2015). As opposed to aquifer thermal energy storage (ATES) and borehole thermal energy storage (BTES) which use the underground environment as a storage medium, cavern thermal energy storage (CTES) which utilizes a cavern as a thermal energy storage tank, is technically feasible even under poor geological conditions, and it can be customized for various purposes and storage temperatures. Moreover, the increasing needs for large-scale high-temperature TES for industrial purposes can make CTES superior to above-ground TES systems. Underground spaces can offer a viable and economical alternative for large-scale storage because the surrounding rock functions as a heat insulator due to its low thermal conductivity (Park et al. 2013). A numerical study of the heat loss characteristics of rock cavern TES and above-ground TES by Park et al. (2014) showed that the heat loss rate of the rock cavern TES approached a certain value with time, whereas that of the above-ground TES system remained constant over the operation period. It was also observed that, in terms of the long-term operation period, the heat loss of the rock cavern TES system exhibited less sensitivity and less dependent behaviors related to the insulator performance compared with those of the above-ground TES system, which suggests that regarding the thermal insulator, the initial construction cost and the risk of possible failure according to the cyclic thermal load can be reduced in the underground space. However, at present, only limited applications of CTES are available because of the high investment costs and the environmental impacts. An exception is the Lyckebo rock cavern used for storing hot water of 40 - 90ºC for a heating system in Sweden, which has been operating since 1983 (SKANSKA 1983). In the case of the CTES for high temperatures above 100ºC, feasibility studies on the technologies for high-temperature and large-scale rock caverns have been conducted by the Korea Institute of Geosciences and Mineral Resources (KIGAM) from 2012 to 2014 (KIGAM 2012; KIGAM 2013; KIGAM 2014).

The estimation and control of the thermal, hydrological and mechanical behaviors of storage caverns and the surrounding rock mass is one of the key issues that should be addressed in the

development of technologies for CTES. The repeated thermal charging and discharging could potentially cause temperature changes in the surface water and groundwater and consequent effects on vegetation and the biosphere. Thermally induced mechanical instability of the storage caverns and the surrounding rock mass as well as the long-term characteristics of hydro-thermal multiphase flow and heat transport are also important issues to be investigated.

The present study is aimed at examining coupled thermal-hydrological-mechanical (THM) behavior in the rock mass around a high-temperature thermal energy storage cavern. As a first step toward understanding the coupled processes in the rock mass, we conducted a numerical study in which the operation of a large-scale high-temperature CTES for 30 years was simulated without consideration of insulator material. Then, the effects of the insulator performance were examined with different insulator thicknesses. The multiphase ground water flow and heat transfer in the rock mass surrounding a rock cavern storing thermal energy of 350ºC were analyzed using the TOUGH2-EOS4 module, which can consider water/air mixtures with vapor pressure-lowering effects (Pruess et al. 1999). The coupled processes between the hydro-thermal flow and the mechanical behavior were predicted by FLAC3D (Itasca Consulting Group Inc. 2012) and the TOUGH-FLAC simulator (Rutqvist et al. 2002; Rutqvist 2011).

Section 2 briefly introduces the numerical model and approach, and Section 3 presents the simulation results in terms of thermal-hydrological flow and mechanical behavior in the rock mass; these are then followed by a few conclusions.

2. Numerical model

2.1 TOUGH-FLAC simulator

The TOUGH-FLAC simulator was initially developed by Rutqvist et al. (2002) as pragmatic approach for modeling of THM processes in porous and fractured geological media. It is based on the linking of two existing codes, TOUGH2 and FLAC3D. The TOUGH2 code is a well-established code for multi-dimensional fluid and heat flows of multiphase, multicomponent fluid mixtures, whereas FLAC3D is a widely used commercial code for rock and soil mechanics with thermo-mechanical and hydro-mechanical interactions. The respective merits of both codes have allowed the TOUGH-FLAC simulator to be widely applied to many THM problems in geological media, such as nuclear waste disposal, CO2 injection, geothermal reservoir engineering and energy storage in rock caverns (Rutqvist and Tsang 2012; Tsang et al. 2008; Rutqvist et al. 2015; Kim et al. 2012). In this technique, TOUGH2 and FLAC3D are executed for a compatible numerical mesh, and the calculation results are transferred mutually and repeatedly through external coupling modules. Multiphase pressures and temperatures calculated by the TOUGH2 code are transferred to FLAC3D, and then a quasi-static mechanical analysis is conducted with FLAC3D at the TOUGH2 Newton iteration level. When a

quasi-static state is reached, FLAC3D provides the mean effective stress of each element to TOUGH2 and the stress-induced changes in porosity, intrinsic permeability and capillary pressure are updated for the next calculation in TOUGH2. The procedures to link the two codes are provided in detail by Rutqvist et al. (2002).

The constitutive equation for thermo-hydro-mechanical interaction used in FLAC3D is expressed as follows:

$$\frac{\partial \sigma_{ij}}{\partial t} + \alpha \frac{\partial P}{\partial t} \delta_{ij} = 2G\left(\frac{\partial \varepsilon_{ij}}{\partial t} - \alpha_t \frac{\partial T}{\partial t}\delta_{ij}\right) + \left(K - \frac{2}{3}G\right)\left(\frac{\partial \varepsilon_{kk}}{\partial t} - 3\alpha_t \frac{\partial T}{\partial t}\right)\delta_{ij}$$ (1)

where σ_{ij} and ε_{ij} are total stresses and strains, α is the Biot coefficient, K and G are bulk and shear moduli, α_t is the linear thermal expansion coefficient, and δ_{ij} is the Kronecker delta.

The porosity-mean stress and permeability-porosity relationships used in the present study are empirical models suggested by Davies and Davies (1999) and slightly modified and applied by Rutqvist et al. (2002):

$$\phi = \phi_r + (\phi_0 - \phi_r)\exp(a\cdot\sigma'_M)$$ (2)

where ϕ is porosity, ϕ_0 is porosity at zero stress, ϕ_r is residual porosity at high stress, σ'_M is mean effective stress and the exponent a should be experimentally determined.

$$k = k_0 \exp\left[c\cdot(\phi/\phi_0 - 1)\right]$$ (3)

where k is permeability, k_0 is permeability at zero stress and the exponent c should be experimentally determined.

The capillary pressure is modified with permeability and porosity according to the function by Leverett (1941):

$$P_c = P_{c0}(S_l)\frac{\sqrt{k_0/\phi_0}}{\sqrt{k/\phi}}$$ (4)

where P_c is the capillary pressure, and P_{c0} is the capillary pressure at zero stress as a function of liquid saturation S_l.

2.2 Model configuration and input parameters

The operation of a large-scale high-temperature TES at a shallow depth for a period of 30 years was numerically simulated, and the coupled THM behavior of the surrounding rock mass was examined. The present study places emphasis on the prediction of the behavior of the rock mass surrounding the storage cavern, rather than the rock cavern itself. We modeled a cylindrical cavern with a height of 50 m and a diameter of 20 m on the basis of the conceptual TES model by Park et al. (2014). In their TES model the storage temperature repeatedly changed in the range of 20 to 685°C according to the operation mode, whereas in this study the storage temperature in the rock cavern is set to 350°C, approximately the average value, based on the assumption that an ideal thermal stratification would be maintained inside the storage cavern. By taking advantage of the planes of symmetry, only one-twelfth (30 degrees) of the region of interest was constructed, as shown in Figure 1. The cylindrical model was extended to a radius of 500 m and a depth of 500 m to ensure the boundaries were at a sufficient distance so as not to affect the near-field behavior. For thermal and hydrological analysis in TOUGH2, the planes of OAA'O', OBB'O', AA'B'B and the bottom were assigned Neumann boundary conditions in which the fluxes of mass and heat crossing the surfaces were not allowed. For the top of the model, the atmospheric temperature and pressure (15°C and 1 bar) were assigned and kept constant during the simulation. The initial condition for the thermal and hydrological calculation was established based a steady-state analysis considering the temperature and pressure gradients of 25°C/km and 10 MPa/km, respectively. For the mechanical analysis in FLAC3D, the nodes on the bottom and the plane AA'B'B were fixed in all directions, whereas those on the symmetry planes OAA'O' and OBB'O' were allowed to move only in the vertical direction. The initial in-situ vertical stress was reproduced by gravitational loading, and the ratio of horizontal to vertical stresses was assumed to be 1.0. In our CTES model, the overburden depth was set to 50 m; with respect to the construction and operation costs, as well as for accessibility to the ground facility, it would be desirable to install the storage cavern at a relatively shallow depth if environmental safety can be assured.

The responses of the surrounding rock, including temperature, pressures, liquid saturation, stresses and displacements, were monitored during the calculation at a total of eight points. The locations of the monitoring points are provided in Figure 1. Points P1, P2 and P3 are at a distance of 5 m from the top, bottom and side wall of the cavern, respectively. Point P4 is at a distance of 50 m from the central axis of the cavern in the radial direction. Points P5, P6 and P7 are located at 5 m depth near the ground surface; point P5 is above the center of the cavern; points P6 and P7 are located at distances of 50 and 100 m from the central axis of the cavern in the radial direction.

To determine the thermal and hydrological properties of the rock mass, typical values for massive granite rocks were chosen from the literature (Waples and Waples 2004; Jaeger et al. 2007; Siegesmund and Dürrast 2011). Jaeger et al. (2007) suggested that the expected ranges of permeability

of unfractured rocks would be $10^{-22} \sim 10^{-12}$ m^2 for limestone, $10^{-17} \sim 10^{-11}$ m^2 for sandstone and $10^{-20} \sim$ 10^{-16} m^2 for granite and gneiss. However, the macroscopic permeability of a fractured rock mass is affected by the interconnectedness of the fracture network and is usually greater than the measurement in the laboratory on an intact core. According to de Marsily (1986), the permeability of a fractured crystalline rock would be in the range of 10^{-15} to 10^{-11} m^2 and that of fractured limestone in the range of 10^{-10} to 10^{-8} m^2. In our simulations, a permeability of 10^{-15} m^2 was assigned to the rock mass and a hydrostatic initial pressure was set based on a water table coinciding with the ground surface. As the relative permeability function and capillary pressure function for the rock mass, the van Genuchten - Mualem model (Mualem 1976; van Genuchten 1980; Pruess et al. 1999) and the van Genuchten model (van Genuchten 1980; Pruess et al. 1999) were applied; the parameters for the functions were determined based on Kim et al. (2012). For the mechanical properties of the rock mass, it was assumed that the rock mass quality was fair with an RMR (rock mass rating) of 50 and a GSI (geological strength index) of 45. The cohesion and friction angle of the rock mass were chosen from the RMR system by Bieniawski (1989). The deformation modulus was calculated from the equation by Hoek et al. (2002), with the disturbance factor of zero. Table 1 gives a summary of the input parameters for the numerical model. For the properties of the insulator, a detailed description is provided in Section 3.3.

The elements representing the interior of the cavern were assigned an elastic model and considered only as a heat source having constant temperature (350ºC) during the simulation. In fact, for more accurate predictions of the mechanical behavior of the storage cavern, it might be desirable to consider the excavation process and the ground water flow into the cavern during its construction. However, the mechanical behavior of the cavern was of relatively minor significance in the present study; we focused on the examination of the coupled THM processes occurring in the surrounding rock mass considering the high-temperature heat source.

3. Results of numerical simulations

3.1 Thermal-hydrological flow

The thermal-hydrological behavior of the rock mass induced by thermal energy storage was examined by monitoring the changes in temperature, pressure and liquid saturation over the operation period. Figure 2 shows the temperature contours of the surrounding rock, which were estimated at 1 year, 3 years and 30 years after the start of the operation. Figure 3 shows the calculated temperature variations at the monitoring points during the operation period.

As shown in Figure 2, as the simulation time proceeded, the temperatures in the surrounding rock increased to over 100ºC; the distances between the cavern walls and the zones having a temperature of 100ºC were 9 m after 1 year, 15 m after 3 years and 33 m after 30 years. The temperature contours

exhibited a radial gradient around the cavern, which indicated that the heat flow was dominated by conduction and that the effects of groundwater were not significant. Temperatures in proximity to the storage cavern (at P1, P2 and P3) increased rapidly and tended to approach certain values at an early stage of the operation. At a distance of 50 m from the central axis of the cavern (at P4), there was a minor change in the temperature until 5 years, but the temperature gradually increased to approximately 75ºC after 30 years. Near the ground surface (at P5, P6 and P7), the temperatures showed relatively minor variations, which might be attributed to their proximity to the atmospheric boundary condition.

In reality, there is heat transfer from the ground surface to the air that can be modeled with a heat transfer boundary condition that regulates the heat flow from the surface to the ambient air. Such a heat transfer boundary condition is considered in the building physics when calculating heat transfer between the buildings and the outside air through the ground. There is a heat transfer coefficient between the air and the ground surface that depends, for instance, on wind conditions, and its value ranges from 5 to 50 W/m²K (Bergman et al. 2011). In the TOUGH2 simulation, we modeled such heat transfer conditions by setting the thermal conductivity of a thin layer boundary element. These are 1 m thick elements with the connection distance of 0.5 m to the next (rock) elements below. To represent a heat transfer coefficient ranging from 5 to 50 W/m²K, the thermal conductive of the boundary elements should be 2.5 to 25 W/mK. These are values on the same order as or much higher than the rock thermal conductivity (3.0 W/mK) in this case. In practice, this means that the ground surface temperature will stay constant at 15□C and that the constant temperature boundary condition at the ground surface is realistic. However, it is worth noting that the rock temperature at a depth of 5 m was still increasing at the end of the simulation, as shown in Figure 3. A preliminary study to examine the long-term thermal transfer showed that it would take several hundred years for the rock mass to reach a steady temperature. Considering the uncertainties of the input parameters and the limitation of continuum modelling, there are potential impacts on near-surface vegetation and the biosphere during the operation period.

Figure 4 shows the liquid saturation contours of the surrounding rock estimated at 1 year, 3 years and 30 years after the start of the operation, and Figure 5 shows the pressure contours at the same stages. As time proceeded, the rock temperature around the storage cavern increased over the boiling temperature, which caused evaporation and a decrease in liquid saturation. Interestingly, there was no significant evaporation and its effect on the pressure even in the regions having a temperature > 150□C. The reason for this lack of thermal-hydrological response is the effect of fluid pressure on the boiling temperature of water. At 100 m depth, the hydrostatic initial pressure was approximately 1 MPa, according to the ground water table at the surface. The boiling point of water is greater than 150□C, approximately 180□C, at a pressure of 1 MPa, as shown in Figure 6. An unsaturated zone was already formed in the early stage within 5 years and did not show significant change until the final

stage. Around the storage cavern, the increase in fluid pressure following evaporation at the early stage raised the boiling point, which, in turn, prevented evaporation at the later stage.

Figure 7 compares the numerical results with and without consideration of the stress-dependent rock mass properties: the variations of temperature, pressure and gas saturation monitored at P3 during the first 10-year operation period. Simulations with TOUGH2 overestimated the temperature, pressure and gas saturation compared to the simulations with TOUGH-FLAC, even though there were no significant differences. As described in Section 2, the porosity, permeability and capillary pressure are directly corrected or indirectly affected by mean effective stress in the TOUGH-FLAC simulation. Thermally induced stress concentration lowered the porosity and permeability, impeding heat transfer and water flow through the rock mass.

3.2 Mechanical behavior

In this section, the mechanical responses of the surrounding rock mass to the thermal and hydrological processes resulting from thermal energy storage are presented. The main geo-mechanical responses are driven by thermal expansion which is expected to cause ground surface uplift and stress changes within the rock mass. The change in fluid pressure is also an important factor affecting the effective stress around the storage cavern. Generally, it is expected that the fluid pressure would decrease effective stress, whereas thermal stress would increase effective stress.

Figure 8 shows the increments of the mean total stress, mean effective stress and pressure after 30 years of operation. In these contours, compressive stresses have a positive sign. Increases in stresses and pressure can be clearly observed in proximity to the storage cavern; the maximum values of the increments are 17.1, 14.5 and 3.6 MPa, respectively. From the results in Figure 8 it can be concluded that the calculated change in effective stress was mainly attributed to thermal stress and stress concentration at the side wall. The effects of pressure and evaporation were found to be relatively minor.

Figure 9 shows the amount of total displacement and the vertical and horizontal displacements after 30 years. The ground-surface uplift was approximately 10 mm after 1 year and 23 mm after 3 years, and it reached 90 mm after 30 years. Uplift greater than 10 mm was found over a wide area above the cavern: the zones extending approximately 150 m from the center of the model.

Figures 10 and 11 provide the magnitude and direction of the effective principal stresses around the storage cavern, respectively. The compressive stress developed around the cavern, and the maximum values of the major and minor compressive effective principal stresses were 22.5 MPa and 12.8 MPa, respectively, at 30 years. The effective principal stresses showed overall radially graded distributions due to thermal expansion. There was an exception in the proximity to the ground surface; tensile stress developed as minor effective principal stress near the ground surface as a result of the free moving boundary condition at the top of the model; a low level of compressive stress was

9

distributed as a major effective principal stress in a direction parallel to the ground surface. At the side walls, a high level of major effective principal stress developed in the tangential direction and the minor effective principal stress developed in the radial direction, as shown in Figure 11; this could bring about some shear failure and local damage. The planes of the major and minor effective principal stresses were parallel to the XY plane (see the axes in Figure 1).

Figure 12 shows the effective principal stress paths at the monitoring points over the operation period, along with the Mohr-Coulomb failure envelope; the yellow circles denote the respective final stages. In FLAC3D, the Mohr-Coulomb model can be used with tension cutoff; the shear failure and tension failure are defined by the following two criteria, respectively.

$$\sigma'_1 = \sigma'_3 N_\phi + 2c\sqrt{N}, \quad N_f = \frac{1 - \sin\phi}{1 + \sin\phi} \tag{5}$$

where σ'_1 and σ'_3 are major and minor effective principal stresses, ϕ is the friction angle and c is the cohesion

$$\sigma'_3 = \sigma_t \tag{6}$$

where σ_t is tensile strength.

At the monitoring points P1, P2 and P3 located at a distance of 5 m from the storage cavern, both principal stresses increased with time due to thermally induced stress. The changes in stresses occurred rapidly in the early stage and there were minor changes after 5 years. The exception is that the stresses at P1, in particular the minor effective principal stress, decreased after 1 year; this might be attributed to uplift of the regions above the storage cavern. At point P4, the major effective principal stress increased consistently in the radial direction, but the minor effective principal stress decreased for the first 5 years and increased with rock heating (see Figure 3). The direction and magnitude of the minor effective principal stress were affected by differential deformation as a result of heating and uplift of the surrounding rock mass. The decrease in the minor effective principal stress in the early stage could cause mechanical instability by increasing the deviatoric stress, even though in this particular case the stress state was below the failure envelope.

The effective principal stress states at the points P5 and P6 reached the shear failure envelope after 3 years and 9 years from the start of operation, respectively. The major effective principal stress slightly increased because of the shallow overburden and small temperature change, whereas the minor effective principal stress decreased with the development of tensile stress following the uplift of the ground surface. It is expected that the stress state at P7 would reach the shear failure envelope if

the operation continued beyond 30 years. Tensile failure was not observed in any element because the tensile strength of the rock mass was set to 5.0 MPa. However, tensile failure close to the ground surface could also be expected, considering that the main reason for the shear failure was the development of tensile stress.

The effective principal stress state of each element within the model was examined by calculating the strength-stress ratio. The strength-stress ratio is defined as the ratio of the maximum allowable major effective principal stress $\sigma'_{1,\,max}$ under the current minor effective principal stress σ'_3 to the current major effective principal stress σ'_1, where the $\sigma'_{1,\,max}$ can be obtained from Eq. 5. The ratio is always greater than or equal to 1.0, and the region with a higher ratio is considered more stable state in terms of shear failure. Figure 13 shows the contours of the strength-stress ratios estimated at 1 year, 3 years and 30 years after the start of operation; the elements with ratios greater than 10.0 are drawn in the same color. Figure 14 shows the shear yielding zones estimated at 1 year, 3 years and 30 years after the start of operation.

Within a few months of the start of the operation, shear failure began at the side walls of the cavern in the direction parallel to the XY plane, as mentioned above, and then expanded to a zone near the ground surface above the cavern. It is interesting that the zones falling within the range of a few meters from the cavern had relatively high strength-stress ratios; the strength-stress ratio was getting greater as time proceeded, as shown in Figure 13. This is ascribed to the fact that both principal stresses increased simultaneously in proximity to the cavern, resulting in relatively small deviatoric stress. The strength-stress ratios at more distant zones near the ground surface became lower with time because of the development of high deviatoric stress. The shear failure was detected in a wide range above the cavern near the ground surface. The yielding zones expanded as time proceeded, and reached approximately 90 m from the center of the model in the radial direction.

3.3 Effects of insulator performance

In the previous sections, the results of the simulation without the insulator were discussed. In practice, however, an insulator with appropriate performance would be installed on the walls of the storage cavern to prevent heat loss and to alleviate the thermal impact on the surrounding rock mass and the environment. We conducted additional numerical simulations with different insulator performances. Here, the effects of the steel liner and reinforced concrete for the mechanical stability of cavern were not taken into consideration. As a thermal insulator, mineral wool, one of the most common traditional insulation materials, was considered in the model, and its thermal conductivity was determined to be 0.08 W/m^{2}K based on the literature (Jelle 2011; Fletcher Insulation 2015). The thicknesses of the layer were assumed to be 0.5, 0.75 and 1.0 m.

One problem in the procedure for modeling the insulator layer was that very thin elements around the rock cavern were produced, which could bring about some numerical instability. To overcome this

deficiency, we used the concept of the equivalent thermal conductivity. If we assume that the heat transfer through the insulator is one-dimensional steady state conduction with no internal energy generation, the equivalent thermal conductivity of the insulator can be determined by means of the thermal resistance, the definition of which is the ratio of a driving potential to the corresponding transfer rate (Bergman 2011). The heat transfer through the insulator at the top and bottom walls of the storage cavern can be simplified by the conduction in a plane wall, whereas that through the insulator on the side walls can be simplified by the radial conduction in a hollow cylinder, as shown in Figure 15. The resistance for conduction ($R_{t,cond}$) in a plane and that in the hollow cylinder can be expressed by Eqs. 7 and 8, respectively.

$$R_{t,cond} = -\frac{T_2 - T_1}{q_x} = \frac{x_2 - x_1}{kA} = \frac{t}{kA} \tag{7}$$

where q_x is the heat transfer rate in the x-direction , T_1 and T_2 are the temperatures of the wall surfaces at $x = x_1$ and $x = x_2$, respectively, k is thermal conductivity, and A and t are the area and thickness of the wall normal to the direction of heat transfer.

$$R_{t,cond} = -\frac{T_2 - T_1}{q_r} = \frac{\ln(r_2 / r_1)}{2pLk} = \frac{\ln(1 + t / r_1)}{2pLk} \tag{8}$$

where q_r is the heat transfer rate in the radial direction , T_1 and T_2 are the temperatures of the wall surfaces at $r = r_1$ and $r = r_2$, respectively. k is thermal conductivity, and L and t are the length and thickness of the hollow cylinder.

In terms of thermal resistance, we can represent an identical thermal performance with different thicknesses of insulator. For example, the insulator having a thermal conductivity of 1.0 W/mK and a thickness of 1 m has the same thermal performance as the insulator having a thermal conductivity of 0.5 W/mK and a thickness of 0.5 m, according to Eq. 7, if the other conditions are identical with respect to the conduction in a plane. In short, the equivalent thermal conductivity k_e for a fixed thickness of t_e that corresponds to a thermal conductivity k for a different thickness of t can be expressed by Eq. 9 for the top and bottom walls and Eq. 10 for the side walls of the storage cavern.

$$k_e = k\frac{t_e}{t} \tag{9}$$

$$k_e = k \; \frac{\ln\left(1 + t_e / r_1\right)}{\ln\left(1 + t / r_1\right)} \tag{10}$$

In the numerical models, the thickness of the insulator layer was fixed to 2.0 m, and the thermal performances of thicknesses of 0.5, 0.75 and 1.0 m were represented using the equivalent thermal conductivities listed in Table 2.

Figures 16 to 20 compare the results of the simulations according to different insulator performances; the contours of rock temperatures estimated at 30 years after the start of operation in Figure 16, the variations in temperatures at the monitoring points at P1 and P5 in Figure 17, the principal stress paths at P1 and P5 in Figure 18, the amount of uplift of the ground surface occurring during the operation period in Figure 19 and the strength-stress ratio estimated at 30 years in Figure 20.

Briefly, the overall results indicate, as expected, that the temperatures in the rock mass, the uplift of the ground surface, and the effective stresses around the cavern decreased with the thickness of the insulator, whereas the strength-stress ratio increased with the thickness of the insulator. In all simulations in which the insulator was considered, there was little change in pressure, and no evaporation effect was observed within the surrounding rock mass. The insulator prevented the heat transfer to the rock mass; therefore, the shear failure did not occur around the cavern during the operation. However, when the thickness was less than 1.0 m, shear failures were still observed above the cavern, even though the installation of the insulator delayed the moment at which the tensile stress developed above the cavern. When the thickness was 1.0 m, the temperature of the surrounding rock mass stayed below 100ºC during the operation period except for the zones within a few meters from the sidewall of the cavern. Moreover, there was no significant temperature change near the ground surface.

4. Discussions and Conclusions

In the present study, we numerically simulated the operation of the rock cavern storing heat of 350ºC and examined the coupled thermal-hydrological-mechanical behavior in the surrounding rock mass occurring for 30 years of operation. As a fundamental study to understand the possible processes within the rock mass under high temperature condition, the simulations with or without an insulator were conducted using the TOUGH-FLAC simulator.

Assuming that a thermal storage cavern was placed in fractured crystalline granite rock with reasonable permeability, the temperature around the storage cavern exhibited a radial distribution, indicating the heat flow was dominated by heat conduction within the rock mass. The effects of heat advection with groundwater flow were not noticeable. Around the storage cavern, the evaporation of

13

ground water and the formation of an unsaturated zone were observed in the early stage, but the increase in pressure was not significant in spite of high temperatures (greater than 150ºC) because of the dependency of the water boiling temperature on the fluid pressure. The simulation shows that the temperature near the ground surface could be expected to reach approximately 29ºC after 30 years (from 15 ºC at the initial condition). It could likely be controlled through an appropriated insulator, but the insulator performance should be assured for a long-term period, considering that the evolution of the temperature would still be in a transient state at the end of the operation. The fact that the temperature in the upper part is higher than that in lower part in common TES systems is also a matter for consideration in a further study.

The mechanical behavior characterized by effective stress and displacement was mainly affected by thermal expansion. The effects of pressure change and evaporation of ground water were not significant. Shear failure was observed in proximity to the cavern walls in the early stage due to an abrupt increase in the major effective principal stress at the wall in the tangential direction. In terms of shear failure within the rock mass, however, the thermal stress in the vertical direction was a more important factor than the thermal stress concentration. As time proceeded, the thermal expansion induced the tensile stress near the ground surface, which decreased the minor effective principal stress in the vertical direction, causing the stress state to reach the shear failure envelope. Although tensile failure was not observed in the model, the potential for tensile failure could be expected because the least effective principal stress was nearly zero. The occurrence of uplift on the order of a few centimeters was predicted in a wide range near the ground surface. At a real thermal storage cavern, the application of an insulator would reduce the uplift near the cavern, but reinforcement to improve the stiffness and strength of the rock mass should be considered in the design stage of the thermal energy storage cavern.

In the present study, priority was put on the behavior of the rock mass surrounding a thermal energy storage cavern, rather than the cavern itself. The interior of the cavern was assigned an elastic material and modeled to function only as an impermeable heat source. Therefore, the numerical results predicted in proximity to the cavern may be limited in their representation of real phenomenon. For example, if the cavern is not completely filled with thermal storage medium, the surrounding rock would deform in a different way toward the inside of the cavern because of thermal expansion. The construction sequence and the drainage condition of ground water also can affect the distributions of liquid saturation and pressure at the early stage. For a more accurate analysis of the mechanical stability of the rock cavern, a simulation based on the detailed design of a thermal energy storage system related to its construction and operation, such as storage temperature, depth of cavern, heat storage and transfer medium, insulator system, repeated heat charging and so on are required.

To ensure the applicability of rock caverns to thermal energy storage, there are still numerous challenges related to environmental impacts, as well as the technical problems of the estimation and

control of the coupled behavior of the rock mass and the storage cavern. To assess the environmental impact, the standards for regulating the thermal and hydrological responses of the rock mass should be preferentially established based on the ecological backgrounds and the detailed design of the thermal storage system. In addition, in a future study, more reliable estimates of heat transfer in the underground can be determined by accounting for the potential for the heat transfer by groundwater convection and the effects of the fractures intersecting the storage cavern.

Acknowledgements

References

[1] Bergman TL, Lavine AS, Incropera FP, DeWitt, DP (2011) Fundamentals of heat and mass transfer. 7th edition. Wiley, Hoboken

[2] Bieniawski ZT (1989) Engineering rock mass classifications. Wiley, New York

[3] Davies JP, Davies DK (1999) Stress-dependent permeability: characterization and modeling. Society of Petroleum Engineers, paper SPE 56813

[4] de Marsily G (1986) Quantitative hydrogeology. Academic Press, San Diego

[5] Fletcher Insulation (2015) Technical data sheet for mineral wool slab. http://www.insulation.com.au/ LiteratureRetrieve.aspx?ID=65397. Accessed in 28 July 2015

[6] Hoek E, Carranza-Torres C, Corkum B (2002) Hoek-Brown failure criterion-2002 edition. In: Proceedings of NARMS-TAC conference, Toronto, pp. 267-273

[7] Itasca Consulting Group Inc. (2012) FLAC3D manual: Fast Lagrangian analysis of continua in 3 dimensions – ver. 5.0 manual. Itasca Consulting Group Inc., Minnesota

[8] Jaeger JC, Cook NGW, Zimmerman RW (2007) Fundamentals of rock mechanics, 4th edition. Chapman and Hall, London

[9] Jelle BP (2011) Traditional, state-of-the-art and future thermal building insulation materials and solutions-properties, requirements and possibilities. Energy and Buildings 43: 2549-2563

[10] Kim HM, Rutqvist J, Ryu DW, Choi BH, Sunwoo C, Song WK (2012) Exploring the concept of compressed air energy storage (CAES) in lined rock caverns at shallow depth: A modeling study of air tightness and energy balance. Applied Energy 92: 653-667

[11] Kim H, Park D, Park E, Choi BH (2015) Analysis of pillar stability in thermal energy storage caverns using numerical modeling. Rock Mechanics and Rock Engineering 48: 1737-1743

[12] Korea Institute of Geoscience and Mineral Resources (KIGAM) (2012) Development of technology of CO2 geological storage and securing green energy resources in deep geo-environment (Part III) GP2012-001-2012(1), Republic of Korea

[13] Korea Institute of Geoscience and Mineral Resources (KIGAM) (2013) Development of technology of CO2 geological storage and securing green energy resources in deep geo-environment (Part III) GP2012-001-2013(2), Republic of Korea

[14] Korea Institute of Geoscience and Mineral Resources (KIGAM) (2014) Development of technology of CO2 geological storage and securing green energy resources in deep geo-environment (Part III) GP2012-001-2014(3), Republic of Korea

[15] Leverett MC (1941) Capillary behavior in porous media. Transactions of the AIME 142: 341-358

[16] Mualem Y (1976) A new model for predicting the hydraulic conductivity of unsaturated porous media, Water Resources Research 12: 513-522

[17] Park D, Kim HM, Ryu DW, Choi BH, Sunwoo C, Han KC (2013) The effect of aspect ratio on the thermal stratification and heat loss in rock caverns for underground thermal energy storage. International Journal of Rock Mechanics and Mining Sciences 64: 201-209

[18] Park JW, Park D, Ryu DW, Choi BH, Park ES (2014) Analysis on heat transfer and heat loss characteristics of rock cavern thermal energy storage. Engineering Geology 181: 142-156

[19] Pruess K, Oldenburg C, Moridis G (1999) TOUGH2 User's guide, ver. 2.0. Lawrence Berkeley National Laboratory Report LBL-43134, Berkeley, CA, USA

[20] Rutqvist J (2011) Status of the TOUGH-FLAC simulator and recent applications related to coupled fluid flow and crustal deformations. Computers & Geosciences 37: 739-750

[21] Rutqvist J, Dobson PF, Garcia J, Hartline C, Jeanne P, Oldenburg CM, Vasco DW, Walters M (2015) The northwest Geysers EGS demonstration project, California: Pre-stimulation modeling and interpretation of the stimulation. Mathematical Geosciences 47: 3-29

[22] Rutqvist J, Tsang CF (2012) Multiphysics processes in partially saturated fractured rock: Experiments and models from Yucca Mountain. Reviews of Geophysics 50, RG3006

[23] Rutqvist, J, Wu YS, Tsang CF, Bodvarsson G (2002) A modeling approach for analysis of coupled multiphase fluid flow, heat transfer, and deformation in fractured porous rock. International Journal of Rock Mechenics and Mining Sciences 39: 429-442

[24] Siegesmund S, Dürrast H (2011) Physical and mechanical properties of rocks. In: Siegesmund S, Snethlage R (editors) Stone in Architecture. Springer-Verlag, Berlin, pp. 97-225

[25] SKANSKA (1983) Swedish rock technique: Lyckebo seasonal energy storage plant. SKANSKA Technical Brochure

[26] Tsang CF, Birkholzer J, Rutqvist J (2008) A comparative review of hydrologic issues involved in geologic storage of CO2 and injection disposal of liquid waste. Journal of Environmental Geology 54: 1723-1737

[27] van Genuchten MT (1980) A closed-form equation for predicting the hydraulic conductivity of unsaturated soils. Soil science society of America journal 44: 892-898

[28] Waples DW, Waples JS (2004) A review and evaluation of specific heat capacities of rocks, minerals, and subsurface fluids. Part 1: Minerals and nonporous rocks. Natural Resources Research 2: 97-122

Table 1. Input parameters used in numerical simulation

Input parameter		Value
Young's modulus, E (GPa)		7.5
Poisson's ratio, v		0.3
Friction angle (degree)		35.0
Cohesion (MPa)		2.5
Tensile strength (MPa)		5.0
Dilation angle (degree)		10.0
Saturated rock density (kg/m^3)		2700
Zero stress porosity, ϕ_0		0.01
Residual stress porosity, ϕ_r		0.009
Zero stress permeability, k_0 (m^2)		10^{-15}
Relative permeability function (van Genuchten - Mualem model)	residual liquid saturation	0.02
	residual gas saturation	0.01
	exponent, m	0.595
Capillary pressure function (van Genuchten model)	air-entry pressure (MPa)	1.470
	exponent, m	0.595
Exponent for Eq.(2), a, (1/Pa)		5×10^{-8}
Exponent for Eq.(3), c		22.2
Biot's parameter, α		1.0
Thermal expansion coefficient, α_t (1/K)		10^{-5}

Thermal conductivity, k (W/mK)			3.0
Specific heat, c_p (kg/J·K)			860.0

Table 2. Modeling of insulator layer with different thicknesses

Insulator		Case 1	Case 2	Case 3
Actuality	Thickness, t (m)	0.5	0.75	1.0
	Thermal conductivity, k (W/mK)	0.08	0.08	0.08
Modeling	Thickness, t_e (m)	2.0	2.0	2.0
	Thermal conductivity for top and bottom, k_e (W/mK)	0.320	0.213	0.160
	Thermal conductivity for side wall, k_e (W/mK)	0.299	0.202	0.153
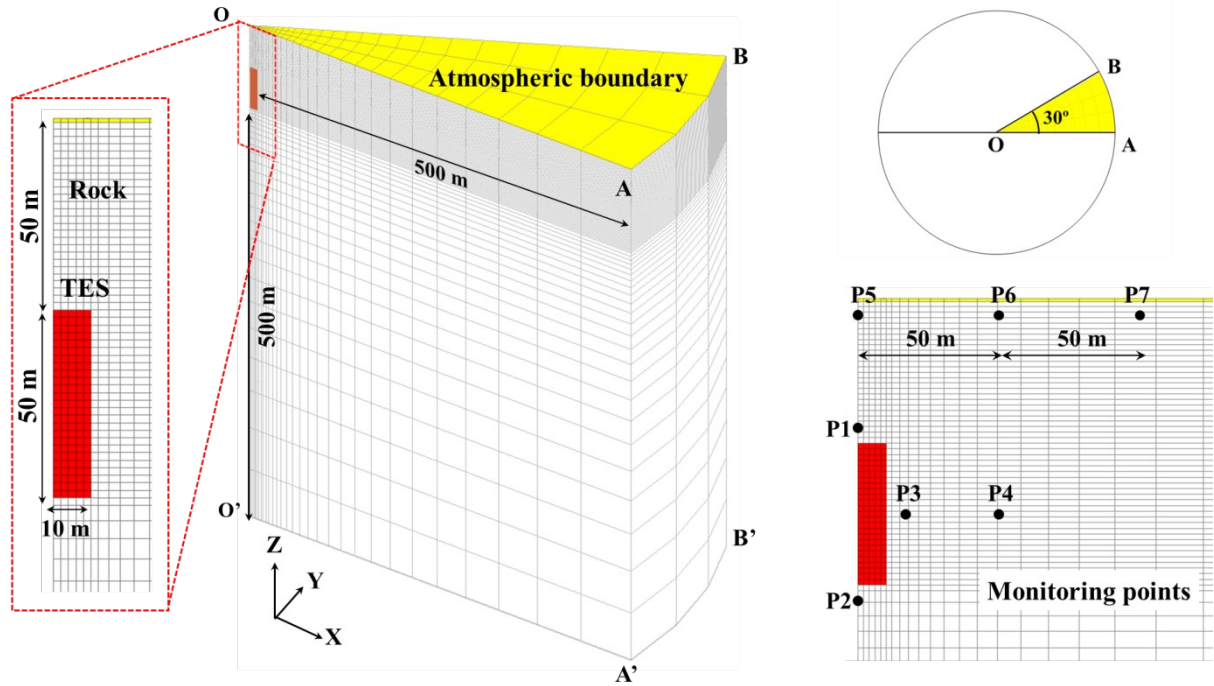
Fig. 1 Symmetrical numerical model and locations of monitoring points
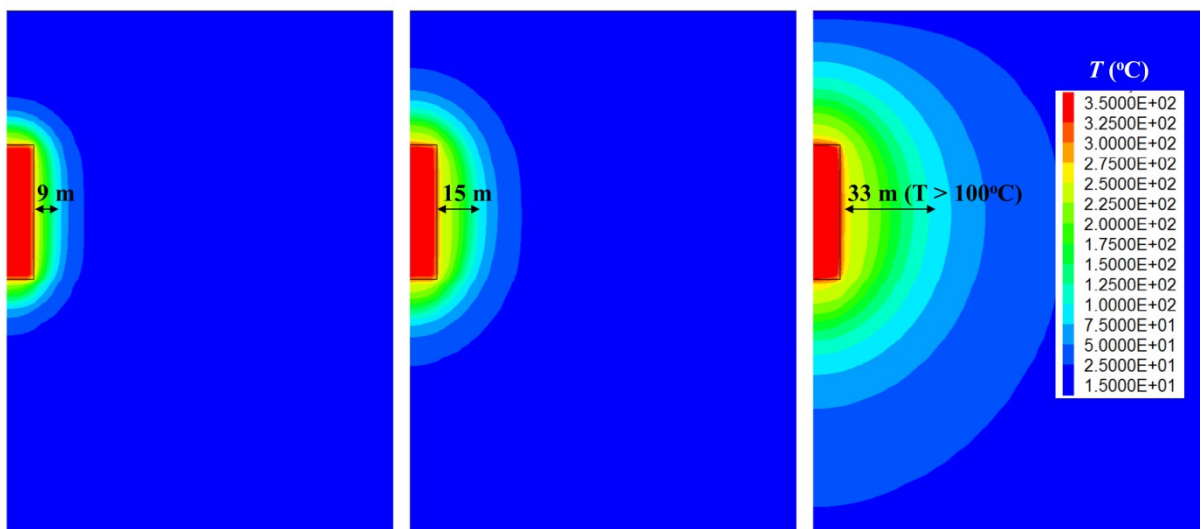
Fig. 2 Temperature (T) contours of the surrounding rock mass estimated at (a) 1 year, (b) 3 years and (c) 30 years after the start of operation
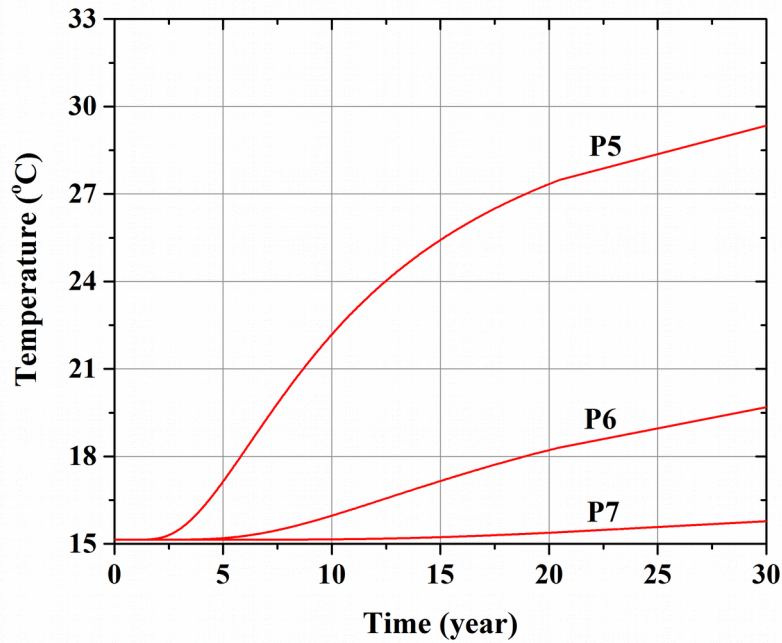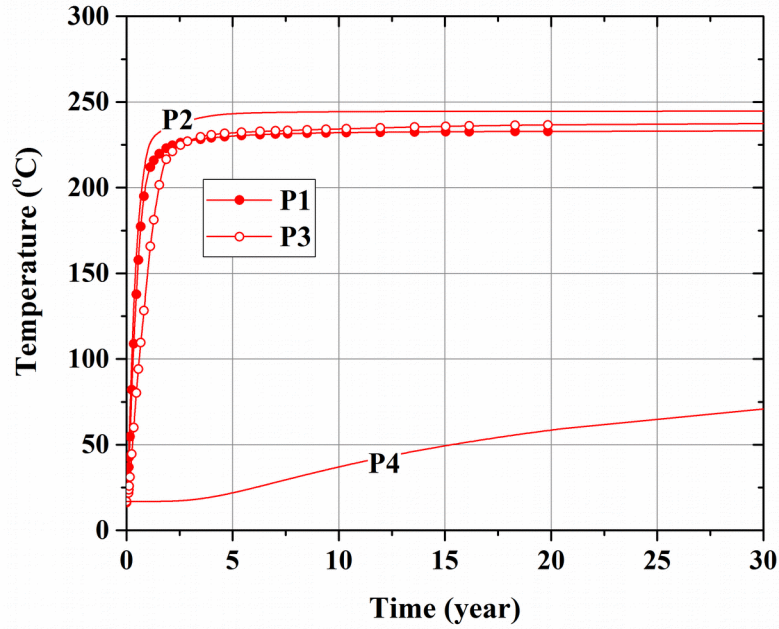
(b)

Fig. 3 Temperatures at the monitoring points (see Fig. 1) over a 30-year operation period
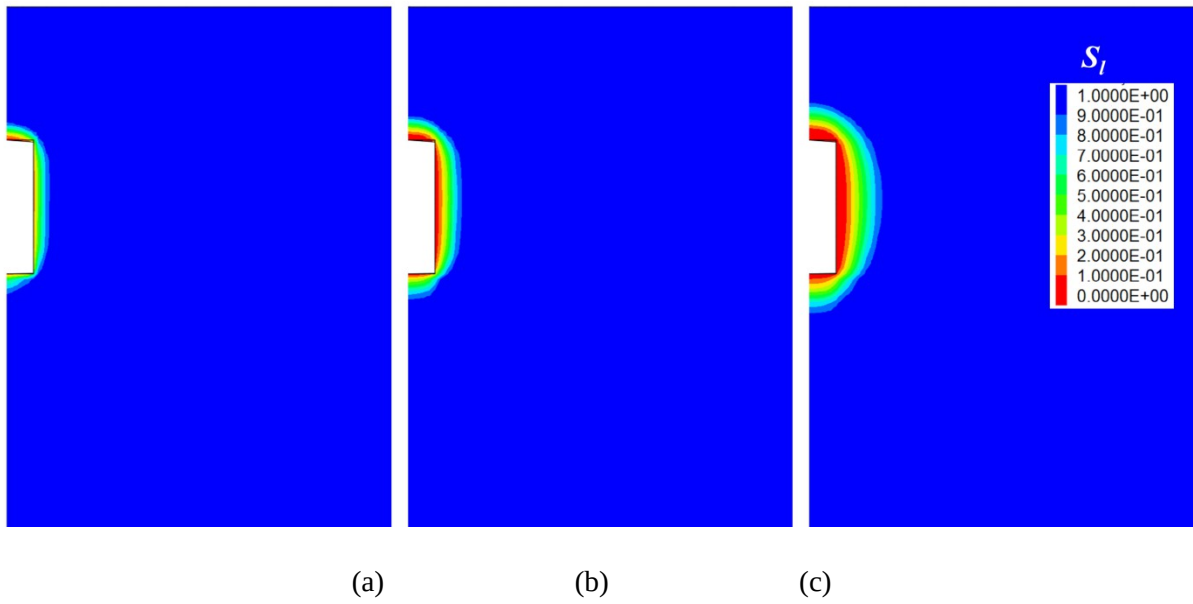
Fig. 4 Liquid saturation (S_l) contours of the surrounding rock mass estimated at (a) 1 year, (b) 3 years and (c) 30 years after the start of operation
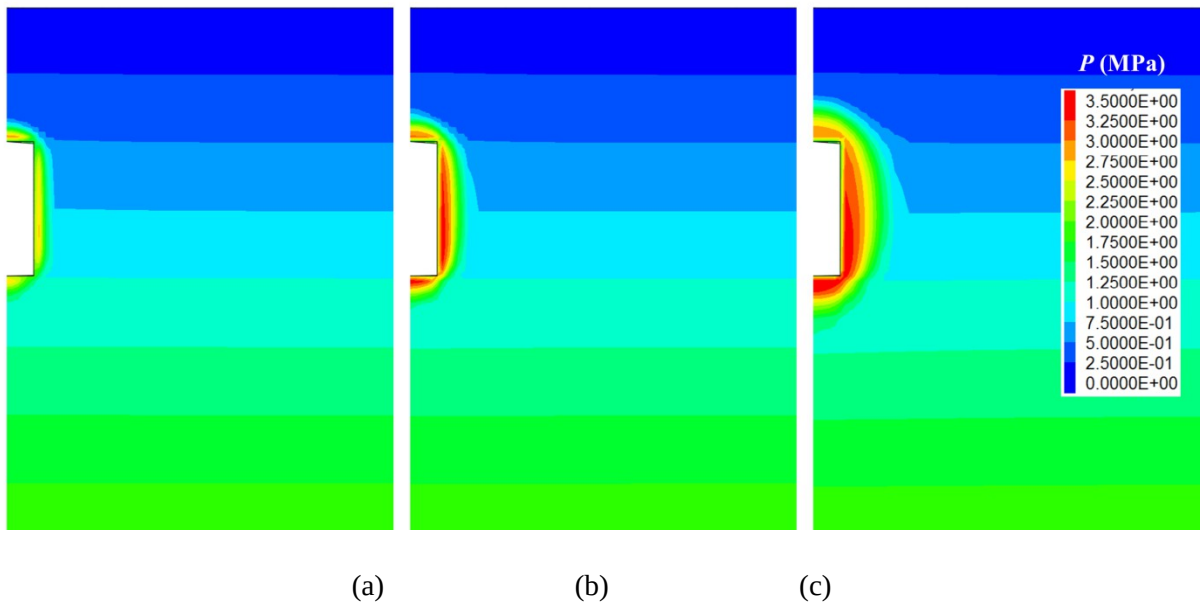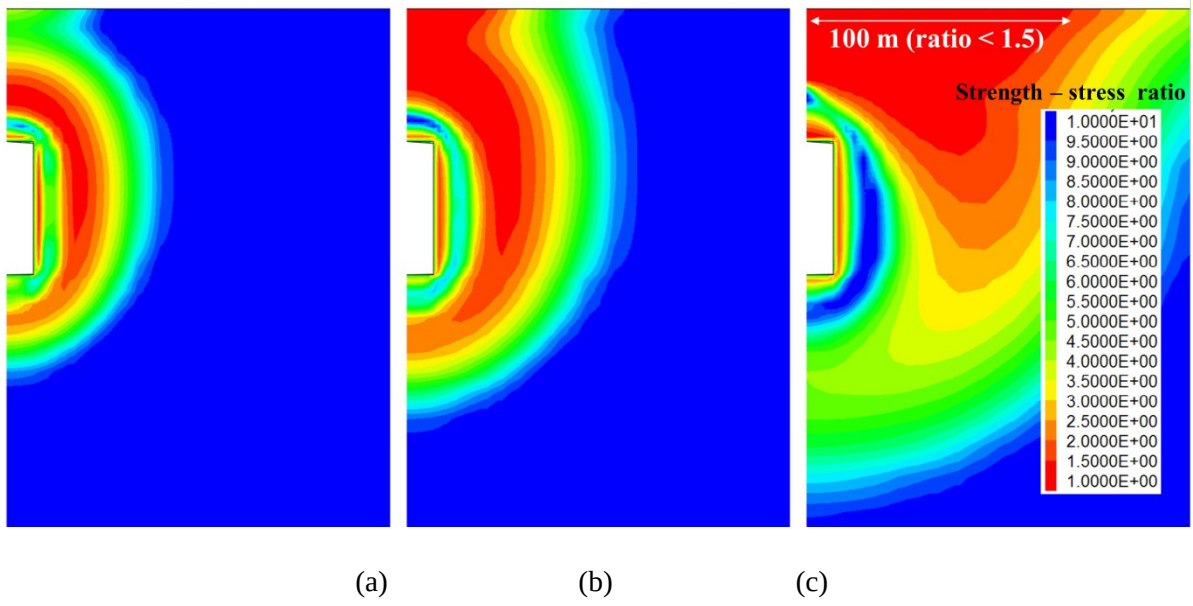

Fig. 5 Pressure (P) contours of the surrounding rock mass estimated at (a) 1 year, (b) 3 years and (c) 30 years after the start of operation
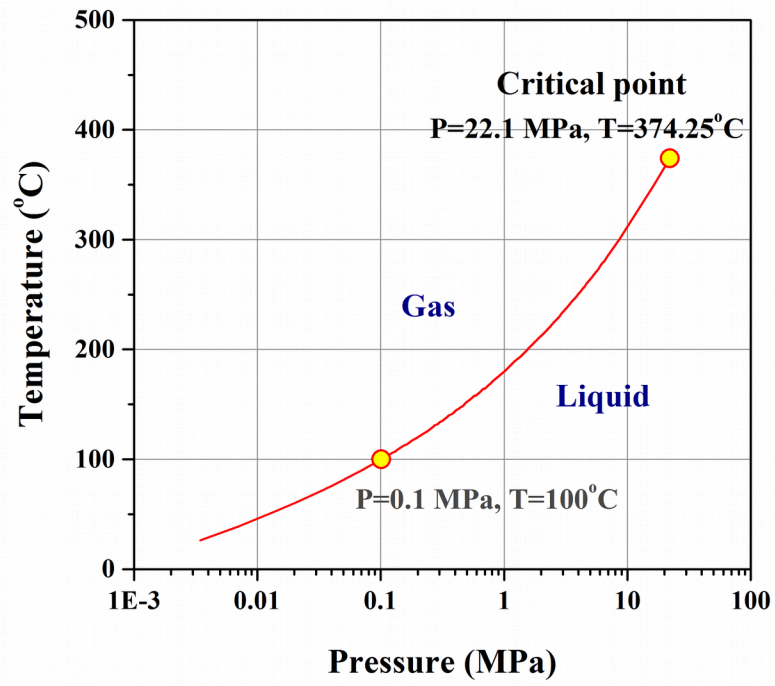
Fig. 6 Variations of water boiling temperature with pressure
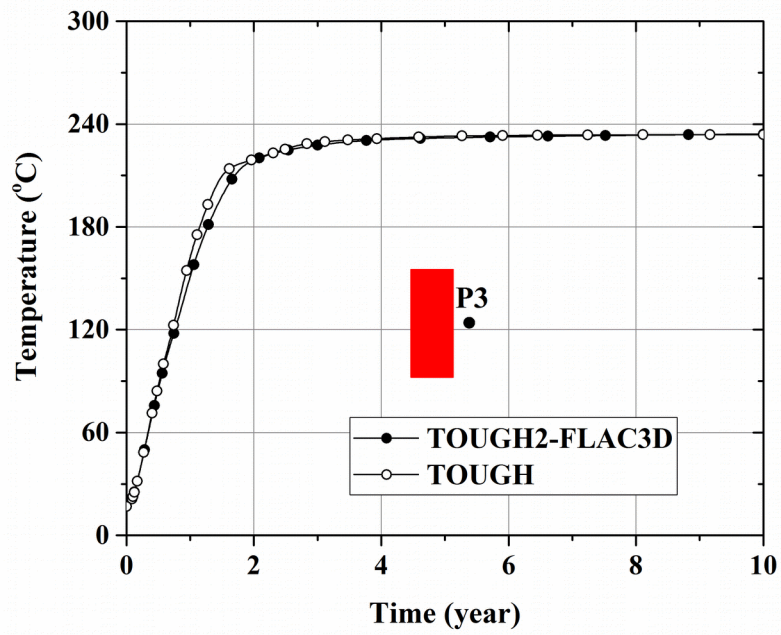
(a)
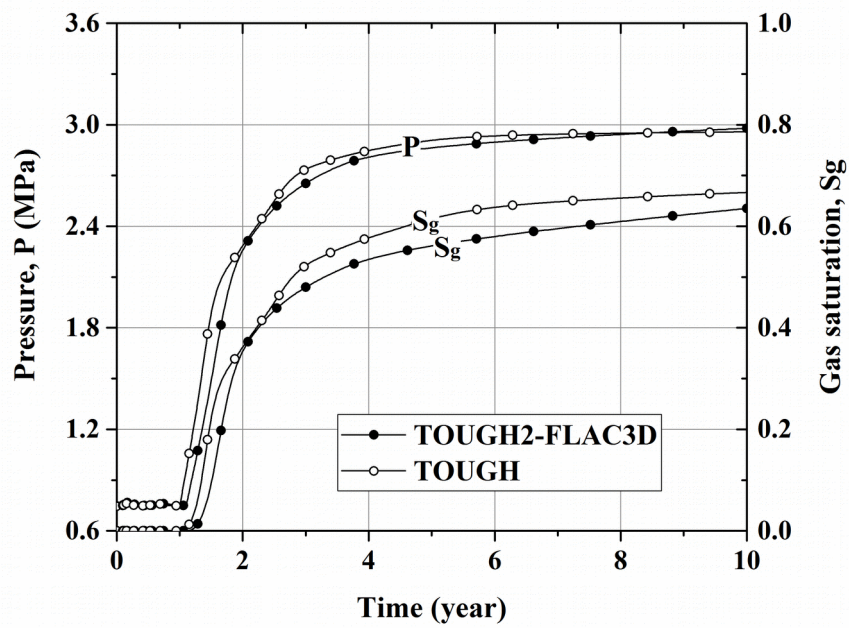
(b)

Fig. 7 Comparisons of the results estimated by TOUGH2-FLAC3D (THM) analysis and those estimated by TOUGH2 (TH) analysis: (a) temperature and (b) pressure and gas saturation monitored at P3

(a)   (b)   (c)
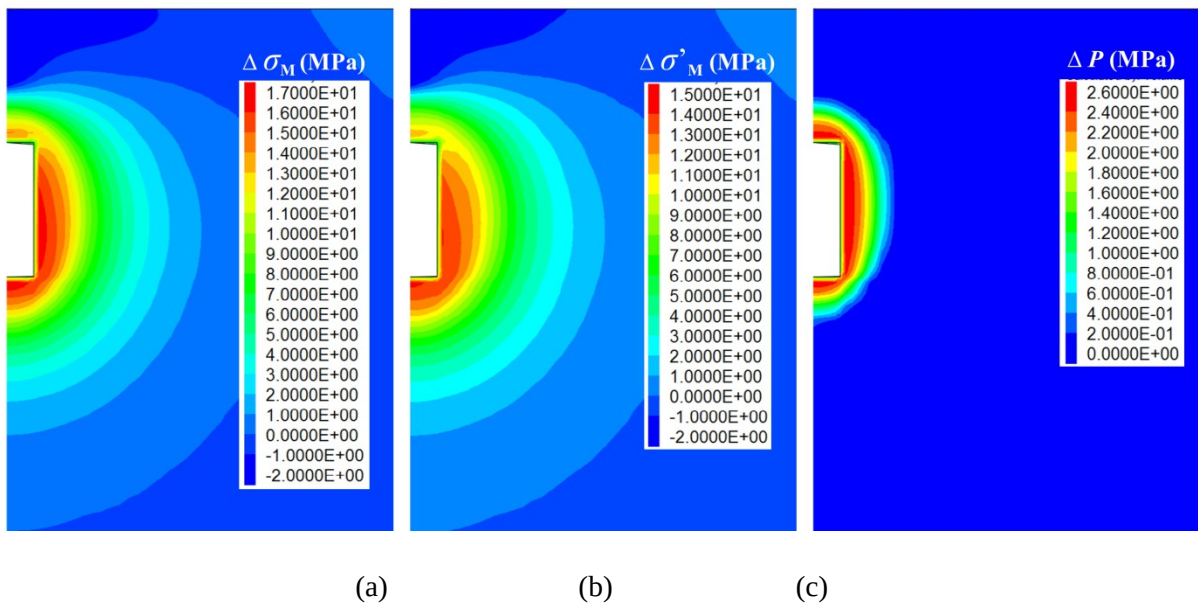
Fig. 8 Increments of (a) mean total stress, (b) mean effective stress and (c) pressure after 30 years of operation; compressive stresses have a positive sign.

(a)   (b)   (c)
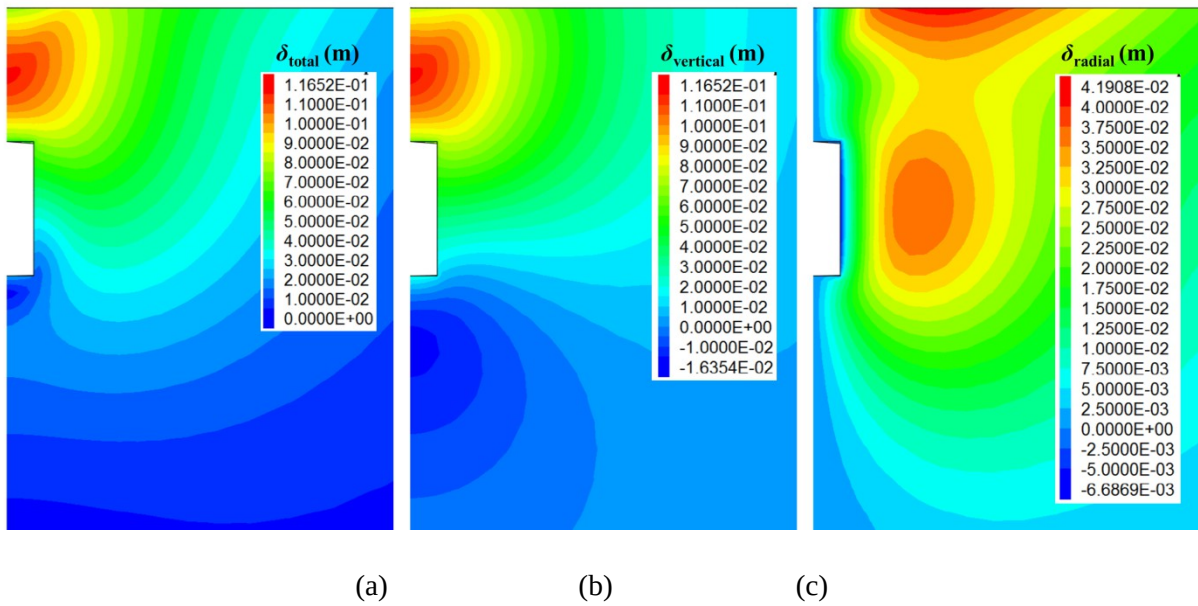
Fig. 9 Displacement contours of the surrounding rock mass estimated at 30 years after the start of operation: (a) amount of total displacement (δ_{total}), (b) vertical displacement ($\delta_{vertical}$), and (c) radial displacement (δ_{radial}); positive signs in (b) and (c) denote upward and rightward movements, respectively.
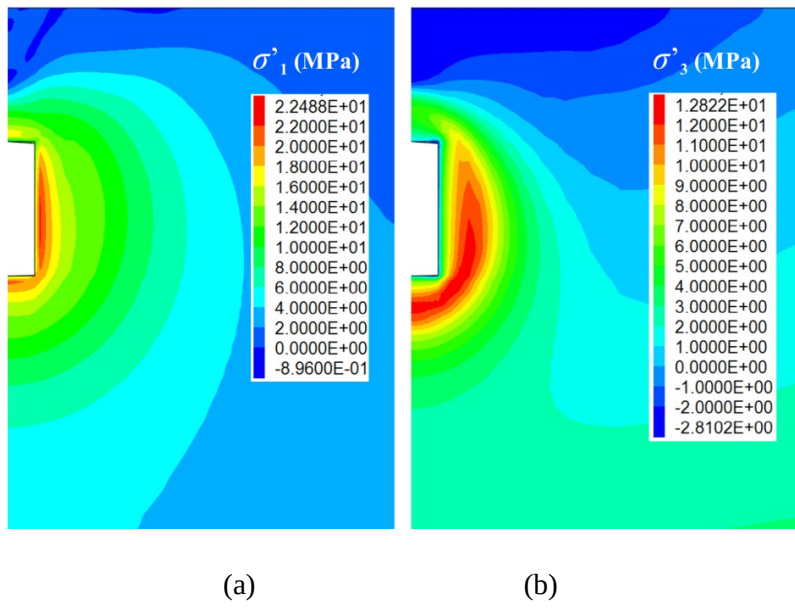
Fig. 10 Effective principal stresses estimated at 30 years after the start of operation: (a) major effective principal stress and (b) minor effective principal stress
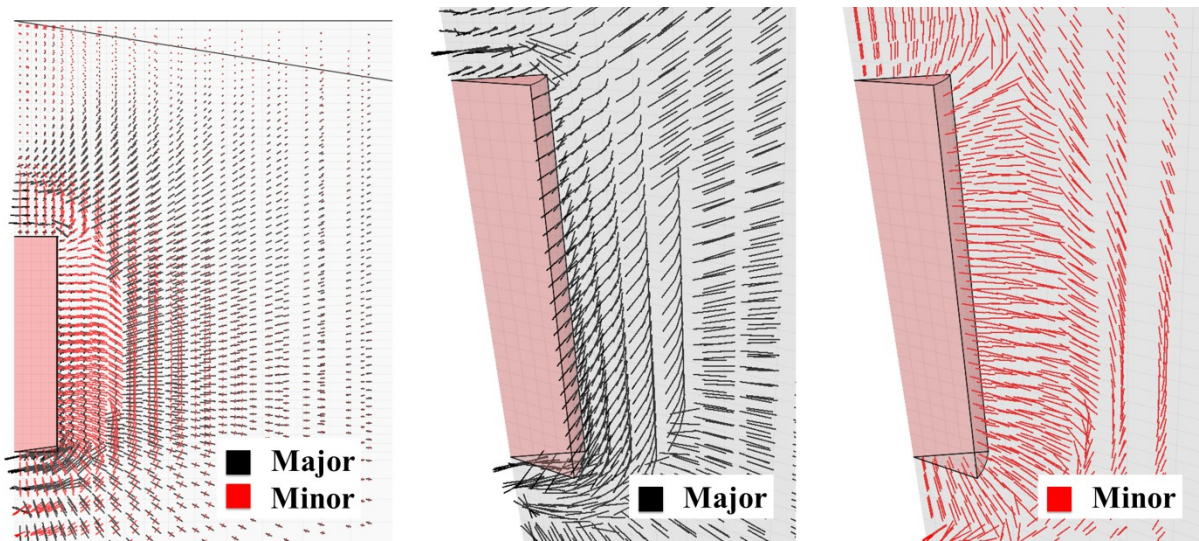
Fig. 11 Directions of major and minor effective principal stresses around storage cavern estimated at 30 years after the start of operation; the length of a line denotes scaled magnitude of stress
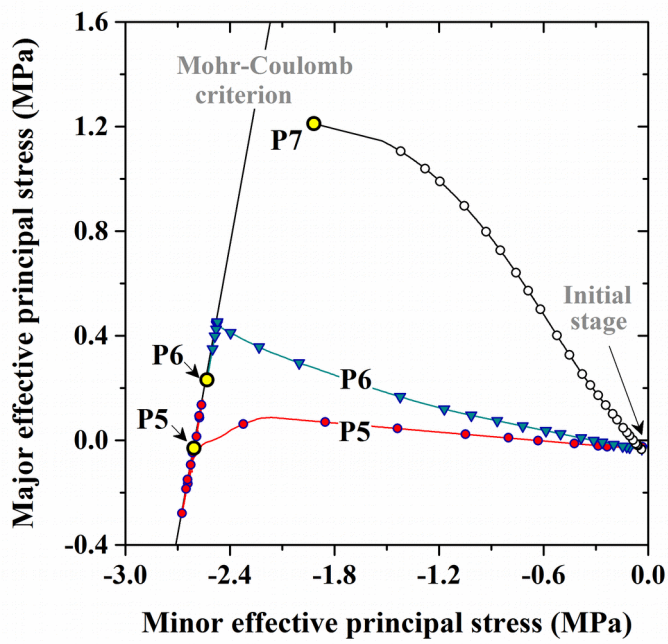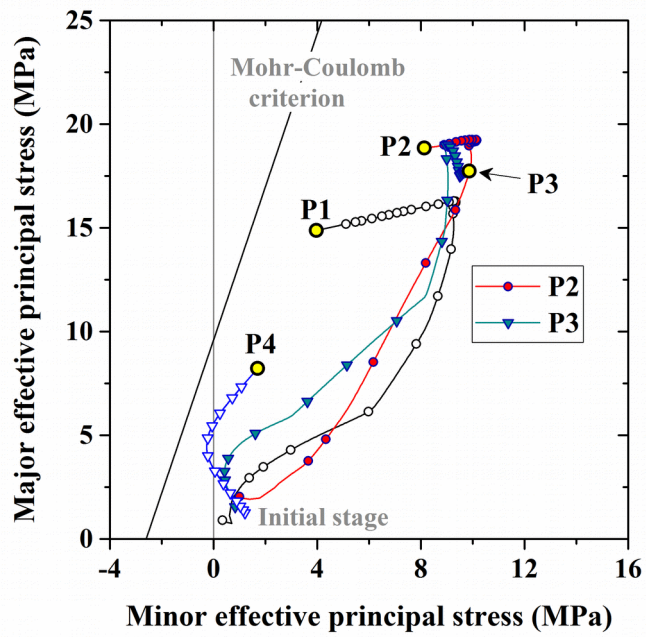
Fig. 12 Principal effective stress paths at monitoring points (see Fig. 1) over a 30-year operation period; the yellow denotes the respective final stage.

Fig. 13 Strength-stress ratio of the surrounding rock mass estimated at (a) 1 year, (b) 3 years and (c) 30 years after the start of operation
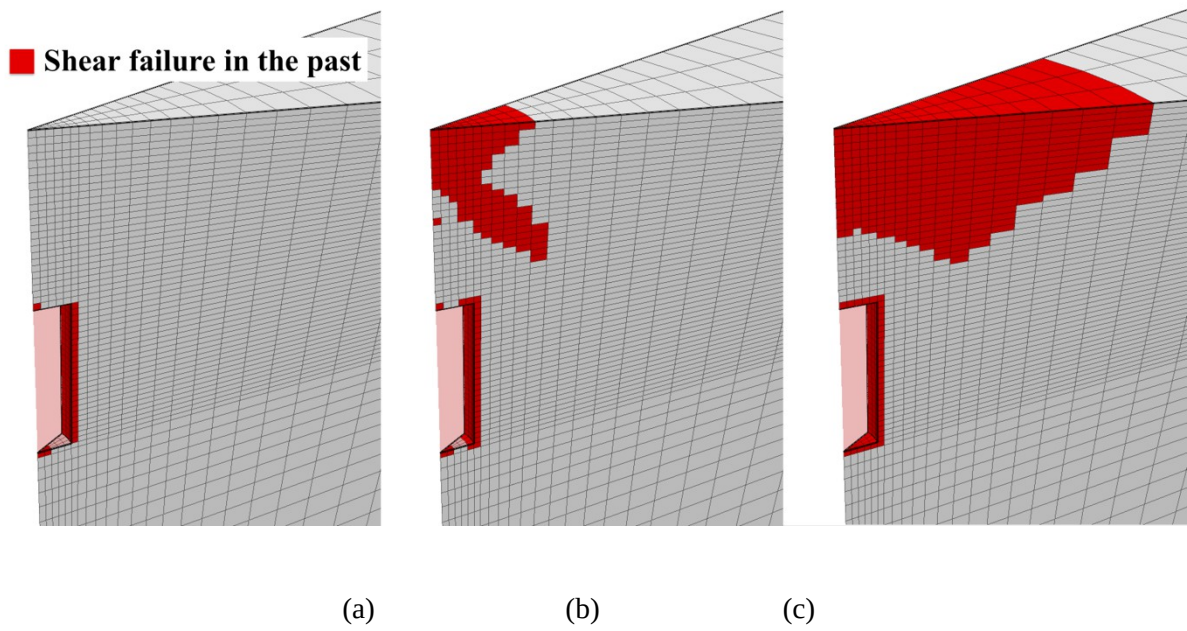
Fig. 14 Shear failure in rock mass estimated at 1 year, 3 years and 30 years after the start of operation

Plane wall
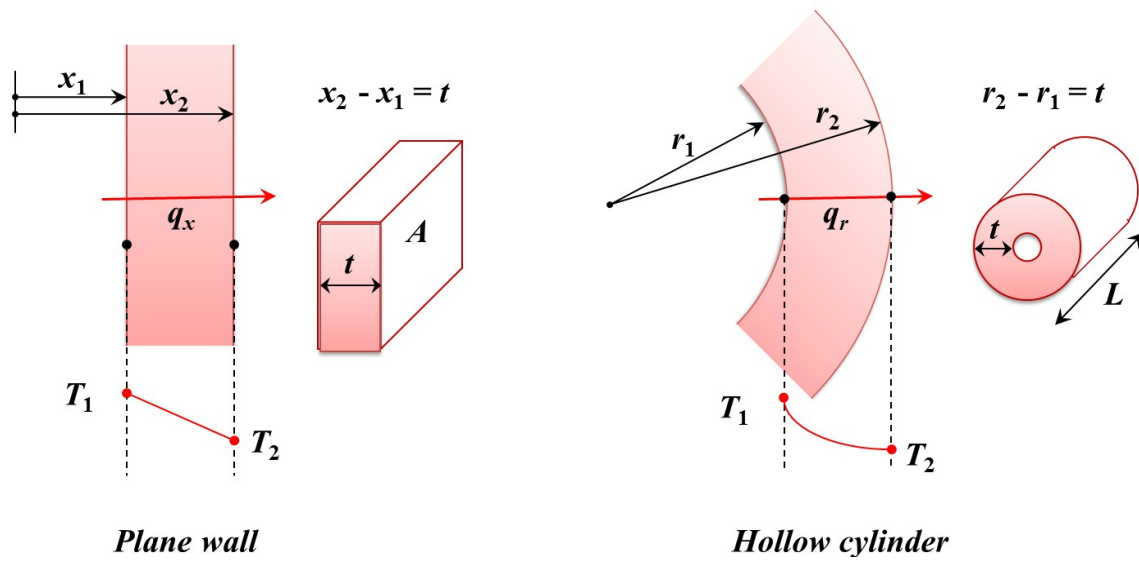
Hollow cylinder

Fig. 15 One-dimensional conductive heat transfer through plane wall and hollow cylinder
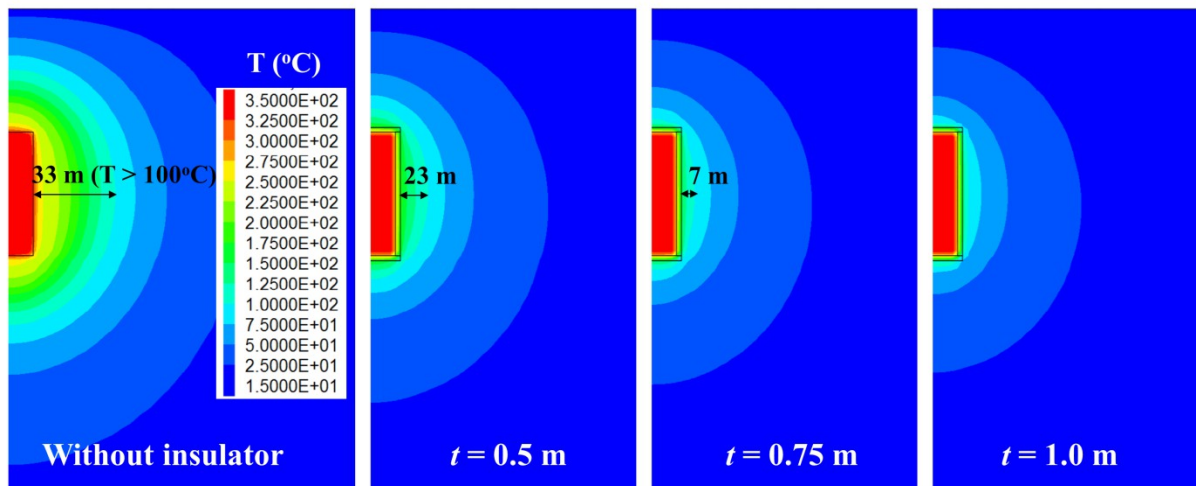
Fig. 16 Temperature (T) contours of the surrounding rock mass estimated at 30 years after the start of operation according to insulator performance; t is insulator thickness.
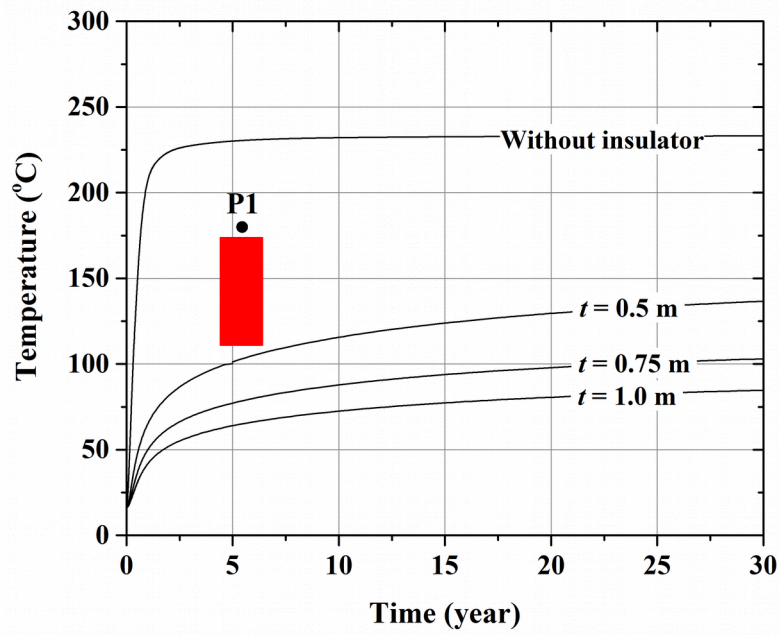
(a)
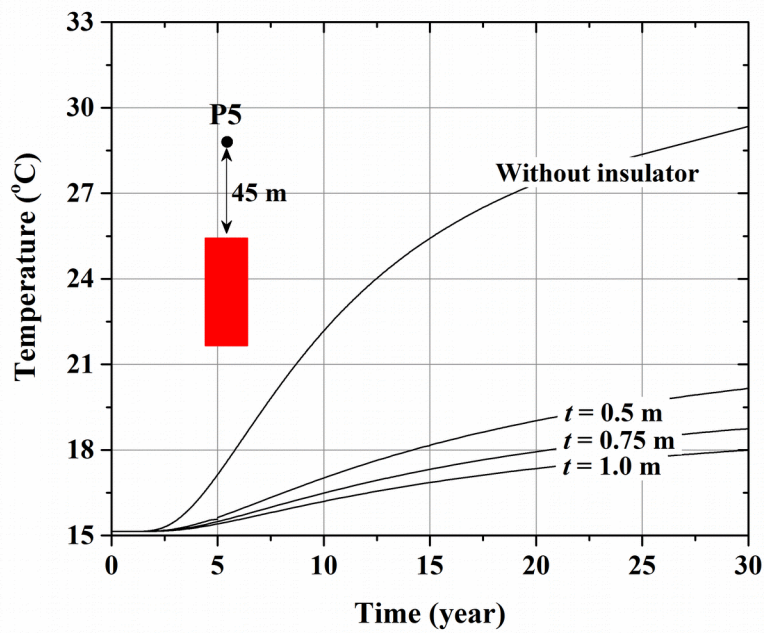
(b)

Fig. 17 Temperatures at the monitoring points (a) P1 and (b) P5 over a 30-year operation period estimated with different insulator performance; *t* is thickness of insulator.
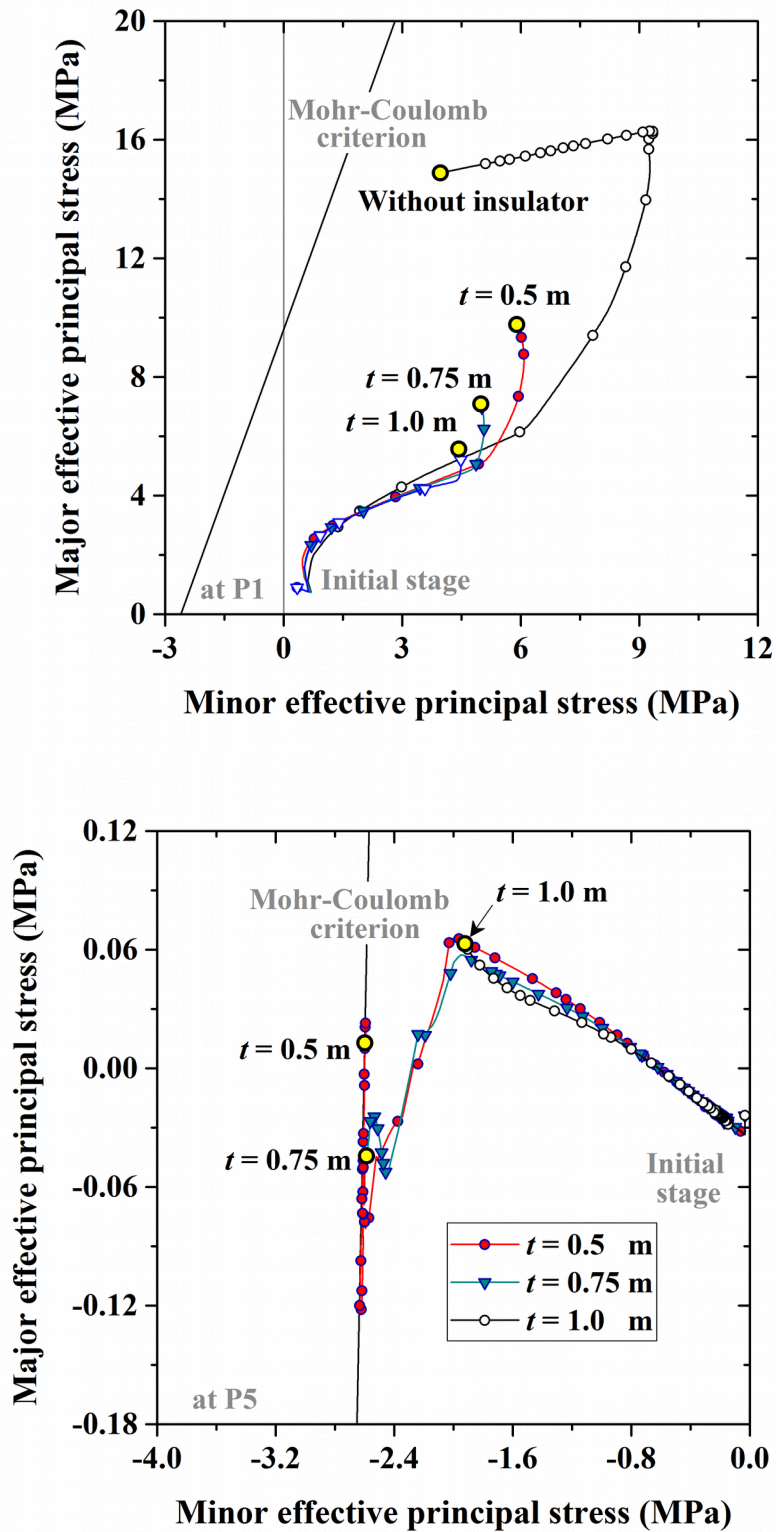
Fig. 18 Effective principal stress paths at monitoring points (a) P1 and (b) P5 over a 30-year operation period according to insulator performance; *t* is thickness of insulator and the yellow denotes the respective final stage.
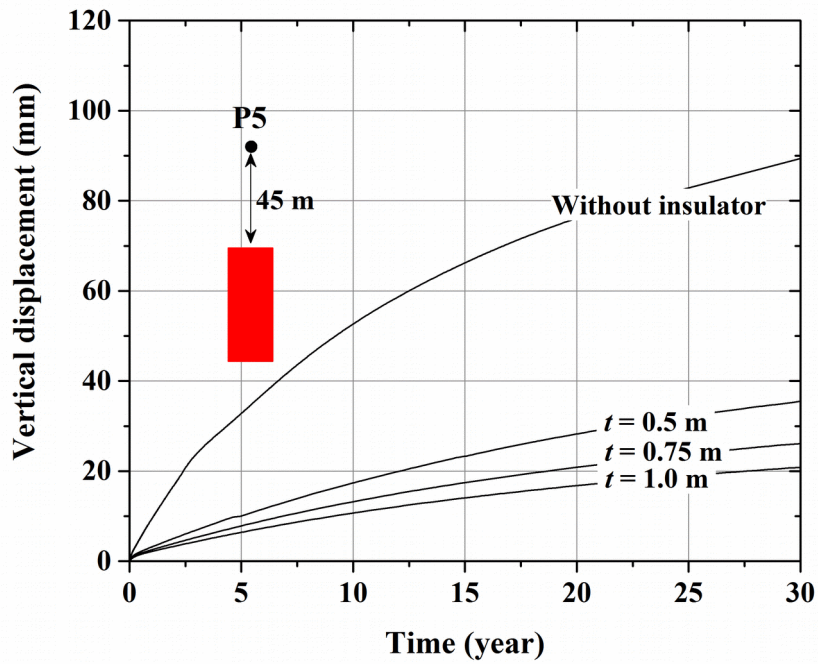
Fig. 19 Vertical displacement at monitoring points P5 over a 30-year operation period according to insulator performance; t is thickness of insulator.
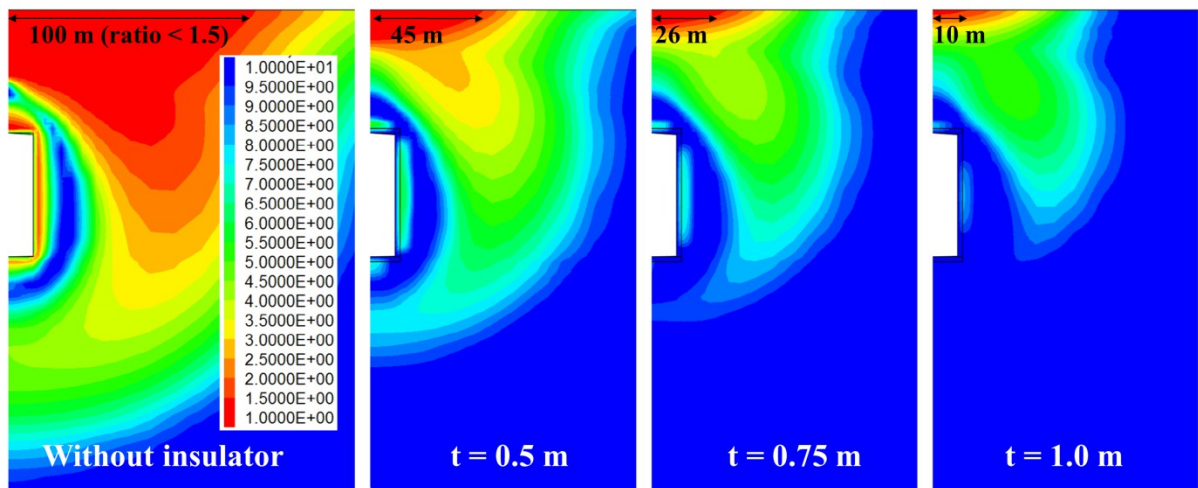

Fig. 20 Strength-stress ratio contours of the surrounding rock mass estimated at 30 years after the start of operation according to insulator performance; t is insulator thickness.

30